Sr dope rutile-RuO_2 for enhanced Proton exchange membrane electrolyzed water

Tianyu Wu, Jinbo Wang, Mengyi Qiu, Yubin Jiang, Chi Song, Junyi Zheng, Ru Chen*

Abstract

As an OER catalyst under acidic conditions, Ir has a high cost and poor activity. Ru is the most promising Ir substitute due to its lower cost and higher catalytic activity, and the development of Ir substitutes has become an urgent need. Herein, we have designed and prepared Sr-doped RuO_2 to achieve an ultra-low overpotential (197 mV@ 10 mA cm^{-2}).In the PEM single cell, a low pool voltage (1.686 V) was achieved at a current density of 1 A cm-^{2}, together with a high stability retention over 400 h of testing. In addition, the catalytic degradation rates (4.63 ng h^{-1}) were significantly lower than those of commercial RuO_2, and the activity is attributed to the increased number of Ru^{3+} active sites and the very small size (5.10 nm). This work provides a new approach for the development of non-Ir-based catalysts with high activity and stability for acidic oxygen precipitation.

Introduction

At present, the most important source of energy for human beings is still fossil energy, however, the global warming problem caused by carbon emissions has greatly affected the living environment of human beings[1]. The development of new energy sources with low carbon emissions has become the goal of many studies. Hydrogen is considered a clean energy source because it produces only water when it releases energy[2, 3]. However, the main methods of hydrogen production now are still accompanied by large carbon emissions[4]. The use of clean energy sources such as wind power and photovoltaic power coupled with electrolysis of water for hydrogen production is ideal for hydrogen production[5, 6]. Currently, the mainstream water electrolysis methods are the following four types: Alkaline water electrolysis (AWE), Proton exchange membrane water electrolysis (PEMWE), Anion exchange membrane

water electrolysis (AEMWE) and Solid oxide electrolyte water electrolysis (SOEWE)[7]. PEMWE has the advantages of high integration, fast startup and shutdown, high hydrogen purity, and is also considered the most ideal way to produce hydrogen[8, 9].

Due to the anode high potential, strong acid caused by the extremely harsh working environment, the anode OER catalyst selection surface is small, only Ir, Ru and other precious metals can ensure high activity[9-11]. The poor activity of Ir-based catalysts and their high price limit their application in PEMWE[12]. It is essential to develop non-Ir OER catalysts[13, 14]. Ru is considered the most promising Ir substitute because of its excellent OER performance and its price[15-17], which is only one tenth of that of Ir. However, it also has the problem of poor activity and stability[18]. To meet the requirements of practical applications, Ru-based catalysts have been modified by doping, loading, etc. Shi et al. modulated the charge structure of Ru by Sn-doped RuO_2 formed solid solution, which substantially improved the stability[19], Wu et al. modified the intermediate evolution mechanism during the OER of Ru-based catalysts by doping the RuO_2 lattice gap with Ni in order to improve the durability of the OER process[20].

Here, we prepared a Sr-doped RuO_2 catalyst. Here, we prepared a Sr-doped RuO_2 catalyst with enhanced OER activity. The as-prepared electrocatalytic electrodes show excellent OER activity in 0.5 M H_2SO_4 (197 mV overpotential at 10 mA cm^{-2}) and long-term stability (more than 400 h at 500 mA cm^{-2}). Excellent activity and stability are proving to be a promising anode catalyst for the electrolysis of water.

2. Experimental

2.1. Chemicals and materials

The chemicals and materials used in this experiment were used directly without any additional processing. Strontium chloride ($SrCl_2$ 99.5%) and sodium chloride (NaCl 99.5%) was purchased from Sinopharm Chemical Reagent Co., Ltd. (shanghai, China). Ruthenium (IV) oxide (RuO_2 98%) was purchased form Adamas-beta® (shanghai, China). Ruthenium(III) chloride hydrate ($RuCl_3$ xH_2O) was purchased from Aladdin Biochemical Technology Co., Ltd. (shanghai, China). Nafion ionomer and proton exchange membrane (N 115), was purchased from Suzhou Sinero Technology.,

Ltd. (Suzhou, China).

2.2. Material synthesis

2.2.1 Synthesis of Sr-RuO_2

In a typical operation, weigh a certain amount of $SrCl_2$ to configure 1 mg/mL $SrCl_2$ solution and weigh amount of $RuCl_3$ xH_2O to configure 20 mg/mL $RuCl_3$ solution. 2 mL $RuCl_3$ solution and 860 μL $SrCl_2$ solution was mixed in 100 mL beaker. After 30 min stirring, add 1.5 g NaCl and 10 mL ultrapure water and then stirring continuously for one hour until completely dissolved. The mixture was placed in a refrigerator for 12 h and then transferred to a freeze dryer for drying. Anneal the mixture in a muffle furnace in 400 ℃ for 2 h. By washing and drying with water, Sr-RuO_2 was obtained.

2.2.2 Synthesis of RuO_2

2 mL $RuCl_3$ solution, 1.5 g NaCl and 10 mL ultrapure water was mixed in 100 mL beaker. The subsequent operation is the same as in 2.2.1

2.3. Characterizations

The X-ray diffraction (XRD) patterns were measured with a powder diffractometer (Bruker D8 Advance) in reflection mode, which was equipped with a Cu-Kα radiation source with an acceleration voltage of 40 kV and a range in 2θ=10°-90°. Catalyst morphology was characterized by spherical aberration-corrected transmission electron microscopy (TEM Themis Z) with high-angle annular dark field – scanning transmission electron microscopy (HAADF-STEM) and energy-dispersive X-ray (EDX) mappings analysis. Analyzing the electronic structure of samples using x-ray photoelectron spectroscopy (XPS Axis Supra) with a monochromatic Al Kα X-ray source. Raman spectra were used in study of the structure of chemical bonds under an excitation of 633 nm laser light in the range of 0-1000 cm^{-1}. Elemental composition of the catalysts was test by ICP-MS.

2.4. Electrode preparation and electrochemical measurements

All electrochemical measurements were performed using the CHI 760E electrochemical work station with three-electrode system. The working electrode was glassy carbon electrode with a calibre of 0.5 cm. A carbon stick as the counter electrode

and a saturated calomel electrode (SCE) as the reference electrode. To prepare the working electrode, 4 mg sample powder was dispersed ultrasonically into the mixture of 500 μL isopropanol, 460 μL Ultrapure water and 40 μL commercial Nafion solution (5 wt.%) to obtain a homogeneous catalyst ink. 10 μL of the ink was drop-casted onto the surface of glass carbon electrode and dried under infrared lamp. The catalysts loading of working electrode was 0.2 mg cm^{-2}. All electrochemical test were using 0.5 M H_2SO_4 solution and in ordinary temperature and pressure.

Before electrochemical testing, the reference electrode was calibrated by using a reversible hydrogen electrode (RHE)[21]. Typically, 0.5 M H_2SO_4 is continuously fed with H_2 for 40 min until the electrolyte is saturated with hydrogen. Two Pt mesh were served as working electrode and counter electrode, SCE as the reference electrode. Using cyclic voltammetry (CV) test between -0.3 V and 0.2 V at a scan rate of 2 mV s^{-1}. The corrected potential is half the sum of the potentials when the oxidizing and reducing currents are 0. In this work, the corrective potential is -0.25 V, so we converted the measure potential to RHE by the following Eq.(1):

$$E_{RHE} = E_{measure} + 0.25\ V \quad (1)$$

The linear sweep voltammetry (LSV) tests were performed at a scan rate of 5 mV s^{-1} with 90 % iR compensation. Tafel slopes were calculated from the polarization curves. Electrochemical impedance spectroscopy (EIS) tests were recorded in the frequency range of 10000 Hz to 0.01 Hz at the 1.45 V (vs. RHE). Double layer capacitance (C_{dl}) was evaluated by CV test at different scan rates (10, 20, 30, 40 and 50 mV s^{-1}) in the non-Faradaic potential range (between 0.98 to 1.08 V vs. RHE). The scan rate is a linear function of the current difference and the slope is the C_{dl}. The electrochemical active surface area (ECSA) can be calculated by means of the following equation:

$$ECSA = \frac{C_{dl}}{C_s} \times AS \quad (2)$$

Where C_s (mF cm^{-2}) is specific capacitance, AS (cm^2) is the electrode's area. In this work, the value of Cs reference to previous studies to be 0.12 mF cm^{-2}.

Chronopotentiometry (CP) measurements were used in stability testing and the current is 10 mA cm^{-2}. The working electrode was Ti mesh coating the catalysts with the cargo of 0.2 mg cm^{-2}.

2.5. PEMWE test

To further validate catalyst feasibility, we use PEMWE cell to evaluate the catalysts' performance. 40% Pt/C was the cathode catalysts with a cargo of 0.5 mg $_{Pt}$ cm^{-2}, Our sample as the anode catalysts with a cargo of 2 mg cm^{-2}. N 115 was the proton exchange membrane without further treatment. Caban paper was used in gas diffusion layer in cathode, Ti fiber paper as the diffusion layer in anodes. To prepare the membrane electrode assembly (MEA), we use catalysts coated membrane (CCM) method. The anodes ink was prepared by the following method: 12.0 mg sample catalysts, 2.5 mL water and 2.5 mL isopropanol were mixed in 5 mL thermos flask, then sonicate and mix for 30 min and add 160 μL ionomer. The cathode ink contains 8 mg Pt/C. Both inks were coated in the two side of porton exchange membrane by sonic spraying in 85℃.

3. Results and discussion

3.1. Fabrication and characterizations of catalysts

Sr-doped RuO_2 was synthesized by salt-sealing method. Specifically, NaCl, $SrCl_2$ and $RuCl_3$ mixed in water and then remove the solvent. The intermediates were oxidized by high temperature via muffle furnace and then remove NaCl by washing with ultrapure water. As a function of the amount of $SrCl_2$ added, we named the resulting samples Sr_2-RuO_2, Sr_4-RuO_2, Sr_8RuO_2 and Sr_{10}-RuO_2. The mass contents of Sr and Ru in the products obtained are analyzed by the ICP-MS method. The ICP results showed that the Sr contents in Sr_2-RuO_2, Sr_4-RuO_2 and Sr_8-RuO_2 were 1.5%, 2.8% and 5.3% (Fig. S1), respectively. Among the as-prepared catalysts, Sr_2-RuO_2 exhibits the highest OER performance in 0.5 M H_2SO_4. Accordingly, most of the characterizations in this paper are focused on this catalyst.

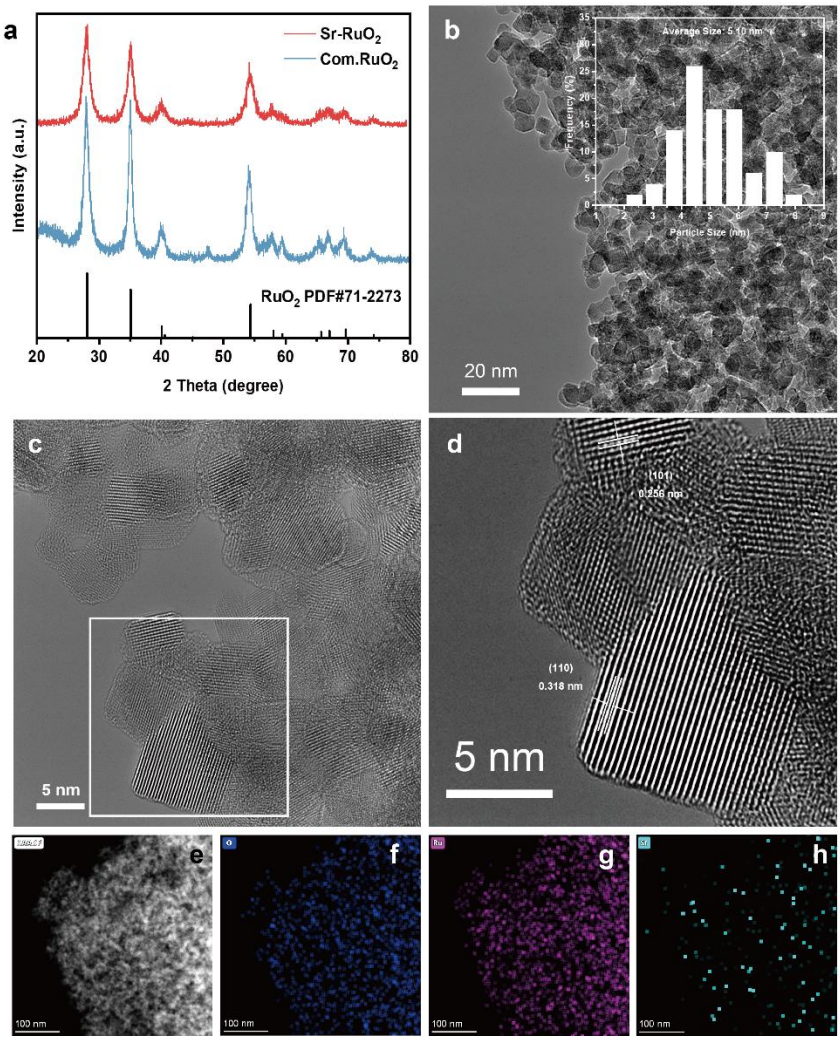

Figure 1. The crystalline structure and morphology of Sr-RuO_2 catalyst. (a) The XRD pattern of the Sr-RuO2 catalyst. (b) The TEM and Particle size distribution statistics of the Sr-RuO2 catalyst. (c, d) The HR-TEM of the Sr-RuO2 catalyst. (e-f) The HAADF and corresponding element mapping images of the Sr-RuO2 catalyst.

As indicated in Fig. 2a, X-ray diffraction (XRD) patterns of RuO_2 and Sr-RuO_2 show the same type of crystal structure attributed to rutile RuO_2 (PDF#71-2273). However, the XRD signal of Sr is not found in the patterns of Sr-RuO_2. This could be related to the low Sr quantity in the catalysts according to the XRD result of Sr_{10}-RuO_2. When the Sr addition is 10 %, a diffraction peak appears at $2\theta = 32°$ (Fig. S2), which corresponds to the perovskite $SrRuO_3$ (PDF#89-5715). There is only one crystallographic peak that shows Sr doping in the RuO_2 lattice. Scanning electron microscopy (SEM) and transmission electron microscopy (TEM) are used for characterization of the morphology of Sr-RuO_2 and RuO_2. The catalysts were found to

be in the form of particles about 10 nm in size, according to the SEM images (Fig.S3). In order to more clearly observe the morphology of the catalyst, the morphology of the sample was characterized by TEM. As shown in Fig. 1b, the Sr-RuO_2 was in the form of particles, and its diameter was 5.10 nm corresponding to the statistics of the particle size distribution. The micromorphology of RuO_2 was in the form of particles as well, only with a larger particle diameter (Fig.S4). From the high-resolution TEM (HRTEM) image of Sr-RuO_2, two types of crystal plane spacings including 0.319 nm and 0.256 nm, attributed to (101) and (110) planes of RuO_2, were clearly observed (Fig. 1d). This was found to agree with the corresponding XRD results. Furthermore, Sr, Ru and O elements are uniformly distributed in the catalyst as shown by the high-angle annular dark-field scanning transmission electron microscopy (HAADF-STEM) image and the elemental mapping results based on energy-dispersive X-ray (EDX). Meantime, the atomic fraction of Sr/Ru is 1.5%, which is close to the result of ICP-MS (Fig.S5).

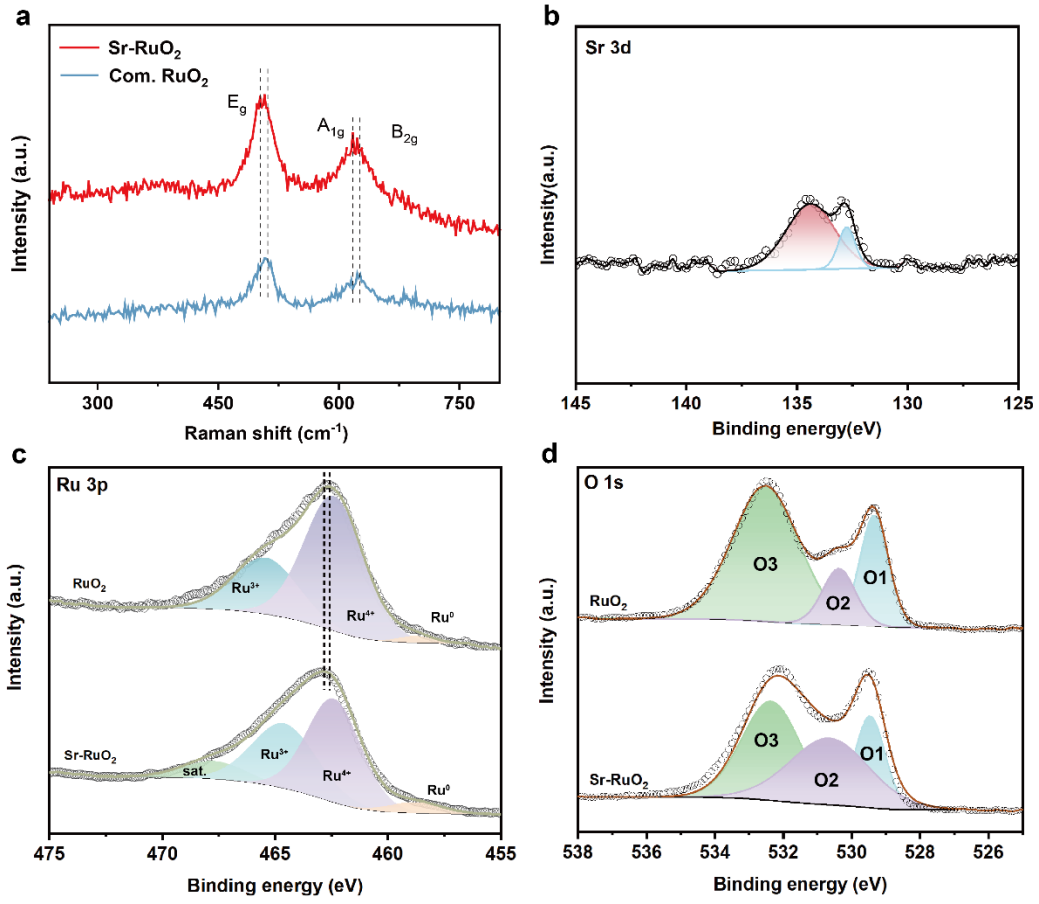

Figure 2. Spectroscopy characterization. (a) Raman spectrum of the catalysts,

(b) XPS Sr 3d spectra, (c) XPS Ru $3p_{3/2}$ spectra, (d) XPS O 1s spectra

The raman spectra of Sr-RuO_2 and RuO_2 were shown in Fig 2a, which two strong peak in 510 cm^{-1} and 626 cm^{-1}, respectively. The peak at 510 cm^{-1} indicates the E_g peak, which is caused by the bending vibrational mode of the Ru-O bonds of rutile RuO_2. The peak around 626 cm^{-1} is the A_{1g} peak caused by the stretching mode of the Ru-O bond in rutile RuO_2[22-24]. Raman peaks related to Sr were not observed, which may be due to the low level of Sr. Meanwhile, it was found that the doping of Sr shifts the RuO_2 Raman peak to red, because the presence of Sr decreases the arrangement degree of RuO_2 chemical bonds[25, 26]. The valence states of different elements in the catalysts are analyzed by X-ray photoelectron spectroscopy (XPS). As shown in Fig. 2b, the Sr 3d spectra of Sr-RuO_2 appear to have two peaks at 134.6 eV and 132.9 eV, which are assigned to Sr $3d_{3/2}$ and Sr $3d_{5/2}$, respectively[27]. Corresponding Sr peaks were measured, demonstrating successful Sr doping in RuO_2. The fine spectrum of Ru 3p shows three peaks of Ru $3p_{1/2}$ (485.15 eV) and Ru $3p_{3/2}$ (463.03 eV) (Fig. S6). Sr doping shifts Ru $3p_{3/2}$ by 0.3 eV in the direction of high binding energy. Ru^{3+} (464.59 eV)), Ru^{4+} (462.40 eV)), and Ru^0 (458.77 eV) were obtained by split-peak fitting analysis of Ru $3p_{3/2}$ (Fig 2c)[28]. The doping of Sr generated more Ru^{3+} sites, which favored the activity[29], and the average valence state of Ru in Sr-RuO_2 was 3.37, lower than that of RuO_2 (3.61). The reason may be that the electron from Sr^{2+} was transferred to nearby Ru sites through bridging oxygen to produce more low valent Ru sites. This enhanced the catalytic activity and stability of OER by modulating the adsorption of oxygen intermediates[30].Three different surface-oxygenated species were deconvoluted at 529.52 eV, 530.52eV, and 532.51 eV. These correspond to the lattice oxygen of Ru-O, the surface OH sites, and the H_2O species, respectively (Fig. 2d). The higher proportion of surface OH sites in Sr-RuO_2 (38.17%) as compared to RuO_2 (22.78%) predicts a higher activity of the OER[31].

3.2. Electrochemical oxygen evolution performance

The OER performances of the electrocatalysts are measured by three-electrode system with 0.5 M H_2SO_4 solution. All the potentials are calculated with respect to the

reversible hydrogen electrode (RHE) with respect to the calibrated SCE reference electrode. The linear sweep voltammetry result show that a low catalytic overpotential (η) of 197 mV is required for Sr-RuO_2 to provide a current density of 10 mA cm^{-2}. This is 110 mV lower than commercial RuO_2. Tafel slope is calculated from the LSV curve. As shown in Figure 3b, the Tafel slope of the Sr-RuO_2 catalyst is 51.1 mV dec^{-1}. The lower the Tafel slope, the higher the electrochemical kinetics.

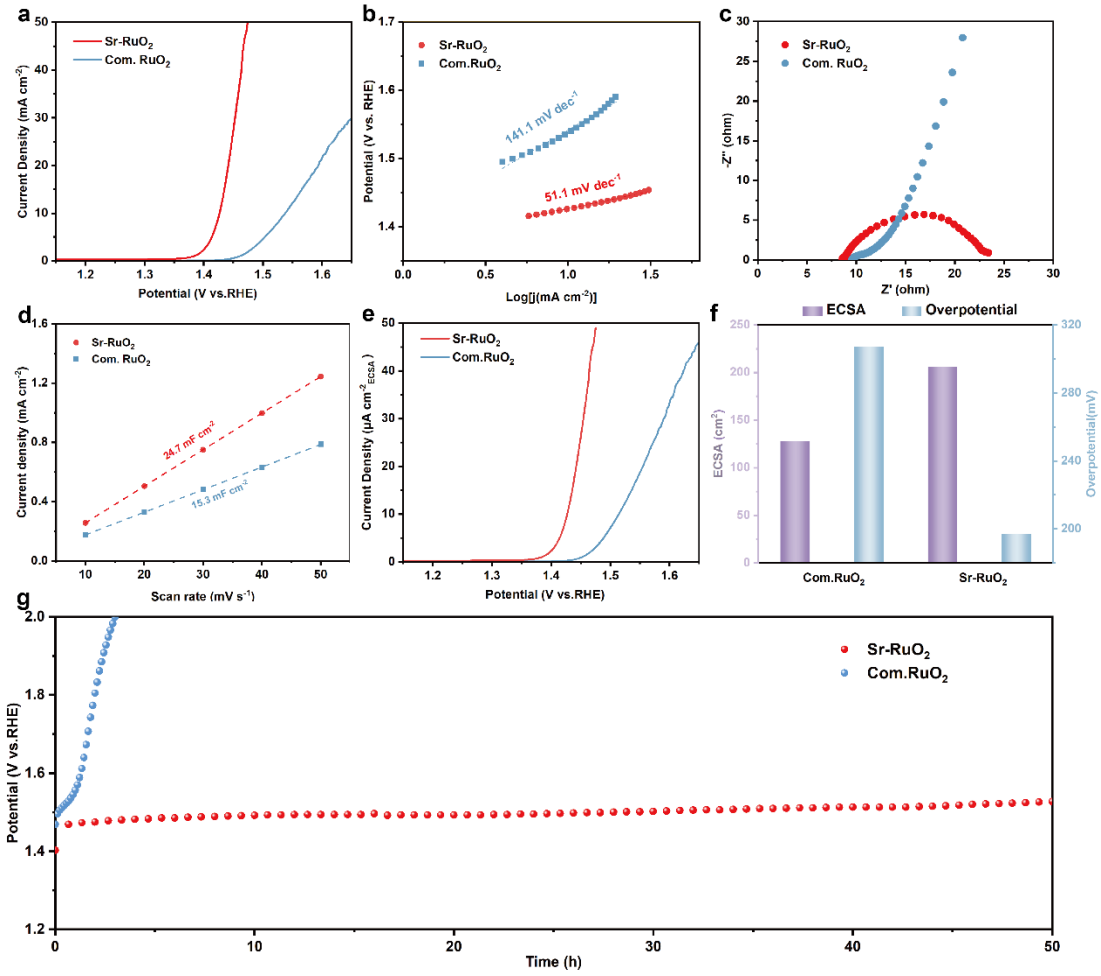

Figure 3. OER performance in three-electrode systems. (a) LSV curves with a scan rate of 5 mV s^{-1} in 0.5 M H_2SO_4 at room temperature, (b) Tafel slop, (c) Nyquist plot of EIS, (d) C_{dl} of catalysts, (e) LSV normalized by ECSA, (f) ECSA and overpotential in 10 mA cm^{-2}, (g) Stability testing in 10 mA cm^{-2}

Charge transfer capability is analyzed by the electrochemical impedance spectroscopy (EIS). The EIS test shown in Figure 3c was performed at an overpotential of 220 mV. EIS is plotted as a Nyquist curve with its intercept on x as ohmic impedance in R_Ω. The R_Ω of Sr-RuO_2 and RuO_2 are similar at 8.8 Ω and 11.5 Ω, respectively. This

indicates that the Sr doping slightly improves the conductivity of RuO_2. The charge transfer resistance (R_{ct}) is obtained by fitting the circuit, and Sr-RuO_2 has a lower R_{ct} (13.9 Ω), while RuO_2 is 582.3 Ω. The lower charge transfer resistance proves that the faster kinetic rate of the Sr doped RuO_2 is higher. Catalyst double layer capacitance (C_{dl}) can be calculated from non-Faraday interval CV studies at different scan rates. C_{dl} of 24.7 mF cm^{-2} and 15.3 mF cm^{-2} for Sr-RuO_2 and RuO_2, respectively, were obtained by linear fitting, with larger C_{dl} indicating the possibility of more active site exposure. The electrochemically active surface area (ECSA) was further calculated from the C_{dl}. The ECSA of Sr-RuO_2 was 205 cm^2, which was about 30% higher than that of RuO_2. This may be due to the smaller particle size. It was found in Fig 3e that the Sr-RuO_2 catalyst also had a higher electrochemical activity, indicating its higher intrinsic activity, using the ECSA-normalizing LSV curves. A constant current test at a current density of 10 mA cm^{-2} was used to test the electrochemical stability (Fig. 3g). In our tests, commercial RuO_2 showed a voltage increase of 500 mV in less than three hours, while Sr-RuO_2 showed an insignificant voltage increase after 50 hours of testing. This proves that Sr-RuO_2 has a higher stability. Simultaneously, the constant CV test method (Fig. S8) was used to test the stability. After 10,000 revolutions of the CV test, we found some variation in the LSV curve before and after, with an overpotential rise of 27 mV at 10 mA cm^{-2}.

For further measurement of the activity and stability of the catalyst under high current conditions, a PEM single cell was used for testing. Commercial 40% Pt/C (0.5 mg_{pt} cm^{-2}) and Sr-RuO_2 (2 mg cm^{-2}) were used as anodes, respectively. Another PEM single cell, constructed with commercial RuO_2, was used for comparison. As shown in Fig. 4a, the PEM cell composed of Sr-RuO_2 has better performance. In particular, cell voltages of only 1.686 and 1.975 V are required to provide current densities of 1 and 2 A cm^{-2}, respectively, far outperforming commercial RuO_2 (1.729 V@1 A cm^{-2} and 2.059 V@2 A cm^{-2}). Electrochemical impedance spectroscopy (EIS) were performed at a cell voltage of 1.6 V and were fitted using the fitting circuit shown in Figure S9. The results show that Sr-RuO_2 corresponds to an anodic R_{ct} of 11.1 Ω in the PEM cell, which is lower than that of RuO_2 (12.4 Ω). This demonstrates higher anodic kinetic rates.

Electrochemical stability was tested at a constant current density of 500 mA cm^{-2} (Fig. 4d), Sr-RuO_2 has a higher stability. Specifically, the pool pressure hardly increased after 400 h of test, whereas commercial RuO_2 rapidly decomposed within a few hours. Catalyst stability was further determined by analyzing the Ru ion content in the effluent water during PEM cell operation using ICP-MS. The dissolution rate of Ru in the Sr-RuO_2 PEM cell was 4.63 ng h^{-1}, which was much lower than that of commercial RuO_2 (28.67 mg h^{-1}). This further demonstrates the higher stability of Sr-RuO_2.

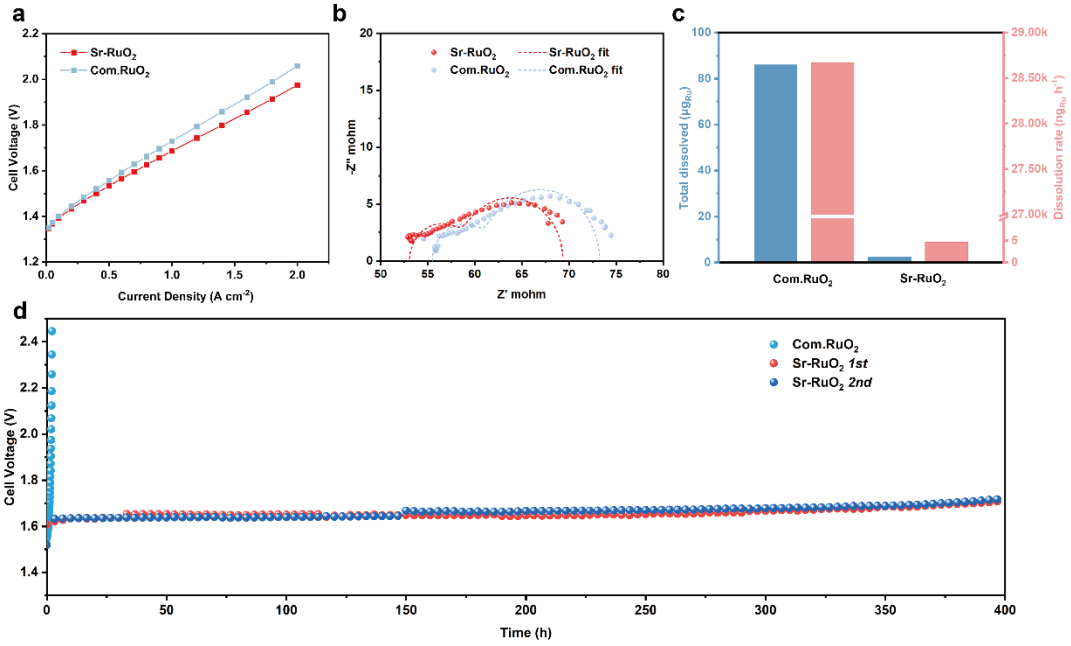

Figure 4. Performance test of PEM water electrolyzers. (a) polarization curve, (b) Nyquist plots and fitting curve of EIS, (c) durability tests at the current density of 500 mA cm^{-2} in PEM water electrolyzers

4. Conclusions

Sr-RuO_2 synthesized using a simple salt capping method has a rutile conformation that maintains RuO_2. It has more Ru^{3+} high activity sites, which is the cause of its high activity. It has high OER activity and stability at 1.5% Sr content. The overpotential (η) is 197 mV at 10 mA cm^{-2}, while only 1.686 V is required to drive a current of 1 A cm^{-2} in a PEM electrolytic cell, while maintaining high stability in a 400h test to a highly promising OER catalyst.

Reference

[1] Allen M R, Frame D J, Huntingford C, et al. Warming caused by cumulative carbon emissions towards the trillionth tonne [J]. Nature, 2009, 458(7242): 1163-6.

[2] Capurso T, Stefanizzi M, Torresi M, et al. Perspective of the role of hydrogen in the 21st century energy transition [J]. Energy Conversion and Management, 2022, 251.

[3] Wappler M, Unguder D, Lu X, et al. Building the green hydrogen market – Current state and outlook on green hydrogen demand and electrolyzer manufacturing [J]. International Journal of Hydrogen Energy, 2022, 47(79): 33551-70.

[4] Dash S K, Chakraborty S, Elangovan D. A Brief Review of Hydrogen Production Methods and Their Challenges [J]. Energies, 2023, 16(3).

[5] Sarker A K, Azad A K, Rasul M G G, et al. Prospect of Green Hydrogen Generation from Hybrid Renewable Energy Sources: A Review [J]. Energies, 2023, 16(3).

[6] Chi J, Yu H. Water electrolysis based on renewable energy for hydrogen production [J]. Chinese Journal of Catalysis, 2018, 39(3): 390-4.

[7] Shiva Kumar S, Lim H. An overview of water electrolysis technologies for green hydrogen production [J]. Energy Reports, 2022, 8: 13793-813.

[8] Carmo M, Fritz D L, Merge J, et al. A comprehensive review on PEM water electrolysis [J]. International Journal of Hydrogen Energy, 2013, 38(12): 4901-34.

[9] Bernt M, Hartig-Weiss A, Tovini M F, et al. Current Challenges in Catalyst Development for PEM Water Electrolyzers [J]. Chemie Ingenieur Technik, 2020, 92(1-2): 31-9.

[10] Sun X, Xu K, Fleischer C, et al. Earth-Abundant Electrocatalysts in Proton Exchange Membrane Electrolyzers [J]. Catalysts, 2018, 8(12).

[11] Xu J, Lian Z, Wei B, et al. Strong Electronic Coupling between Ultrafine Iridium-Ruthenium Nanoclusters and Conductive, Acid-Stable Tellurium Nanoparticle Support for Efficient and Durable Oxygen Evolution in Acidic and Neutral Media [J]. Acs Catalysis, 2020, 10(6): 3571-9.

[12] Liu Y, Liang X, Chen H, et al. Iridium-containing water-oxidation catalysts in acidic electrolyte [J]. Chinese Journal of Catalysis, 2021, 42(7): 1054-77.

[13] Gao J, Tao H, Liu B. Progress of Nonprecious-Metal-Based Electrocatalysts for Oxygen Evolution in Acidic Media [J]. Advanced Materials, 2021, 33(31).

[14] Zhou F, Zhang L, Li J, et al. Novel engineering of ruthenium-based electrocatalysts for acidic water oxidation: A mini review [J]. Engineering Reports, 2021, 3(8).

[15] Danilovic N, Subbaraman R, Chang K-C, et al. Activity–Stability Trends for the Oxygen Evolution Reaction on Monometallic Oxides in Acidic Environments [J]. The Journal of Physical Chemistry Letters, 2014, 5(14): 2474-8.

[16] Sun H, Jung W. Recent advances in doped ruthenium oxides as high-efficiency electrocatalysts for the oxygen evolution reaction [J]. Journal of Materials Chemistry A, 2021, 9(28): 15506-21.

[17] You B, Sun Y. Innovative Strategies for Electrocatalytic Water Splitting [J]. Accounts of Chemical Research, 2018, 51(7): 1571-80.

[18] Fan R-Y, Zhang Y-S, Lv J-Y, et al. The Promising Seesaw Relationship Between Activity and Stability of Ru-Based Electrocatalysts for Acid Oxygen Evolution and Proton Exchange Membrane Water Electrolysis [J]. Small, 2024, 20(5).

[19] Shi Z, Li J, Wang Y, et al. Customized reaction route for ruthenium oxide towards stabilized

water oxidation in high-performance PEM electrolyzers [J]. Nature Communications, 2023, 14(1).

[20] Wu Z-Y, Chen F-Y, Li B, et al. Non-iridium-based electrocatalyst for durable acidic oxygen evolution reaction in proton exchange membrane water electrolysis [J]. Nature Materials, 2022, 22(1): 100-8.

[21] Stevens M B, Enman L J, Batchellor A S, et al. Measurement Techniques for the Study of Thin Film Heterogeneous Water Oxidation Electrocatalysts [J]. Chemistry of Materials, 2017, 29(1): 120-40.

[22] Meng L. Raman spectroscopy analysis of magnetron sputtered RuO_2 thin films [J]. Thin Solid Films, 2003, 442(1-2): 93-7.

[23] Kim M H, Baik J M, Lee S J, et al. Growth direction determination of a single RuO_2 nanowire by polarized Raman spectroscopy [J]. Applied Physics Letters, 2010, 96(21).

[24] Korotcov A V, Huang Y S, Tiong K K, et al. Raman scattering characterization of well-aligned RuO_2 and IrO_2 nanocrystals [J]. Journal of Raman Spectroscopy, 2007, 38(6): 737-49.

[25] Saraswathy R. Electrochemical capacitance of nanostructured ruthenium-doped tin oxide $Sn_{1-x}Ru_xO_2$ by the microemulsion method [J]. Frontiers of Materials Science, 2017, 11(4): 385-94.

[26] Zhang Q, Deng H, Chen L, et al. Cation substitution induced structural transition, band gap engineering and grain growth of Cu_2Cd $Zn_{1-}SnS_4$ thin films [J]. Journal of Alloys and Compounds, 2017, 695: 482-8.

[27] Seitz L C, Dickens C F, Nishio K, et al. A highly active and stable $IrO_x/SrIrO_3$ catalyst for the oxygen evolution reaction [J]. Science, 2016, 353(6303): 1011-4.

[28] Liu H, Zhang Z, Fang J, et al. Eliminating over-oxidation of ruthenium oxides by niobium for highly stable electrocatalytic oxygen evolution in acidic media [J]. Joule, 2023, 7(3): 558-73.

[29] Kim J, Shih P-C, Tsao K-C, et al. High-Performance Pyrochlore-Type Yttrium Ruthenate Electrocatalyst for Oxygen Evolution Reaction in Acidic Media [J]. Journal of the American Chemical Society, 2017, 139(34): 12076-83.

[30] Ge R, Li L, Su J, et al. Ultrafine Defective RuO_2 Electrocatayst Integrated on Carbon Cloth for Robust Water Oxidation in Acidic Media [J]. 2019, 9(35): 1901313.

[31] Chen Y, Liu D, Zhao Q, et al. IrO_x-MoO_3 nano-heterostructure electrocatalysts for efficient acidic water oxidation [J]. Chemical Engineering Journal, 2023, 475.